IEEE Access
Multidisciplinary | Rapid Review | Open Access Journal

Received February 8, 2020, accepted March 13, 2020, date of publication March 17, 2020, date of current version March 26, 2020.

Digital Object Identifier 10.1109/ACCESS.2020.2981548

Design, Analysis, and Test of a Novel 2-DOF Spherical Motion Mechanism

BIN BIAN AND LIANG WANG
School of Automation Science and Electrical Engineering, Beihang University, Beijing 100191, China
Corresponding author: Liang Wang (wangliang@buaa.edu.cn)

This work was supported by the National Nature Science Foundation of China under Grant 50575014.

ABSTRACT A novel two degree-of-freedom (DOF) ball-joint-like hydraulic spherical motion mechanism (SMM) for use in robotic applications is proposed to achieve smooth spherical motion in all directions. Unlike traditional systems that use serial or parallel mechanisms for generating multi-DOF rotations, the proposed SMM is capable of producing continuous 2-DOF rotational motions in a single joint without intermediate transmission mechanisms. The proposed SMM has a compact structure, low inertia, and high stiffness. First, the architecture and operating principle of the proposed SMM is introduced. Then, the kinematic model is established using Euler transformation, following which factors (such as workspace and dexterity) that have an impact on motion performance are evaluated. As the foundation of dynamics analysis and controller design, the Lagrange's equations of the second kind are used to establish the dynamic model. To achieve high tracking accuracy, the radial basis function neural network–based sliding mode controller is applied to the mechanism. The simulation results indicate that the designed controller not only improves trajectory tracking capability but also enhances robustness against external disturbance and system uncertainty. Finally, experiments are performed on a prototype SMM to validate the performance of the proposed SMM and evaluate the control method.

INDEX TERMS Spherical motion mechanism, kinematic modeling, motion performance, dynamic modeling, radial basis function neural network–based sliding mode control.

I. INTRODUCTION

Spherical motion, which is probably the most important type of motion after rotary motion, is a multi-DOF rigid body motion along a spherical surface with a permanent center of rotation. Currently, multi-DOF spherical motions are commonly realized by connecting at least two or three actuators in serial or parallel mechanisms; such a configuration results in transmission systems that are quite complex and bulky [1]–[5], which affects the dynamic performance and servo-tracking accuracy. To overcome these drawbacks, this paper presents a novel 2-DOF ball-joint-like hydraulic spherical motion mechanism (SMM). The SMM, which can achieve smooth spherical motion in all directions with a single joint and without intermediate complex connecting parts, has a compact structure, low inertia, and high stiffness. The SMM could be used in the field of robotics; it could be used as a robotic wrist joint, shoulder joint, hip joint, etc.

The associate editor coordinating the review of this manuscript and approving it for publication was Rui-Jun Yan.

Spherical motion can be achieved by spherical manipulators through either serial or parallel mechanisms. A spherical wrist based on the serial mechanism with four revolute joints was reported in [3]. An SMM designed with serial links was studied in [6]. Furthermore, spherical parallel mechanisms (SPMs) have attracted the attention of many researchers over the last two decades because they have higher stiffness, precision, and load carrying capacity than serial spherical mechanisms. Typical SPMs are the 3-RRR type manipulators, where R stands for the revolute joint [7]–[11]. However, the torsion motion achieved using general symmetrical SPMs is limited. Moreover, SPMs have low positioning accuracy. To overcome these drawbacks, asymmetrical SPMs [12] were proposed. Karouia *et al.* [13] proposed new structural types of asymmetrical non-overconstrained 3-DOF SPMs, which had three limbs of distinct architectures. Wu *et al.* [12] and Wu and Ping [14] designed four types of asymmetrical SPMs, which consisted of an outer ring and an inner ring with a revolute joint.

In addition, redundantly actuated SPMs [15], [16] have been proposed in recent decades; these SPMs allow for an increase in workspace [17], the enhancement of stiffness [18], [19], removal of singularity, and augmentation of dexterity [1], [20]. Many redundantly actuated SPMs have been studied for use in different applications, such as a robotic shoulder [21], wrist [22], and haptic device [23]. Recently, an improved parallel platform with a redundant limb that can adjust the pose in three directions was developed based on the traditional 3RPS parallel mechanism [24]. However, redundantly actuated SPMs require a high number of drivers, resulting in transmission systems that are complex and bulky.

The performance of mechanisms depends on the control algorithms to a certain extent. The system of the SMM is multivariable, strongly coupled, highly nonlinear, etc., which makes it difficult to achieve precise control. In terms of controllers, the traditional PID controller is commonly employed in the industry; however, this type of controller does not always guarantee high performance owing to the complexity and diversity of the system [25]. Sliding mode control (SMC) is an effective nonlinear control method that is currently being used owing to its rapid response and robustness against external disturbance and uncertainty of a system; moreover, it does not depend on a precise dynamic model [26], [27]. Radial basis function neural network (RBFNN) is commonly used to identify the uncertainty and un-modeled dynamics of a system because they can approximate nonlinear functions with proper accuracy [28]–[30]. Therefore, an RBF neural network–based SMC (RBFSMC) is employed to control the SMM.

A novel 2-DOF ball-joint-like hydraulic SMM with an RBFSMC is proposed in this study to achieve spherical motion. The remainder of this paper is arranged as follows:

The architecture and operating principle of the SMM is presented in Section II. The kinematic model is established through Euler transformation in Section III, and the motion is evaluated in Section IV. The dynamic model is derived by Lagrange's equations in Section V. Then, the RBFSMC is designed, and the asymptotic stability of the control system is proven in Section VI. A simulation and experiment are performed to verify the proposed mechanism and evaluate the control method in Section VII. Finally, conclusions are drawn in Section VIII.

II. DESCRIPTION OF THE SMM

Fig. 1 shows the computer-aided design (CAD) model of the SMM, which is a ball-joint-like mechanism, and a prototype SMM was manufactured based on the CAD model shown in Fig. 2.

The architecture of the SMM is shown in Fig. 3. The principal structure consists of two rotors, two stators, a rudder blade, a measurement system, and a hydraulic actuator. The detailed architecture and fundamental operating principle of the SMM is described as follows.

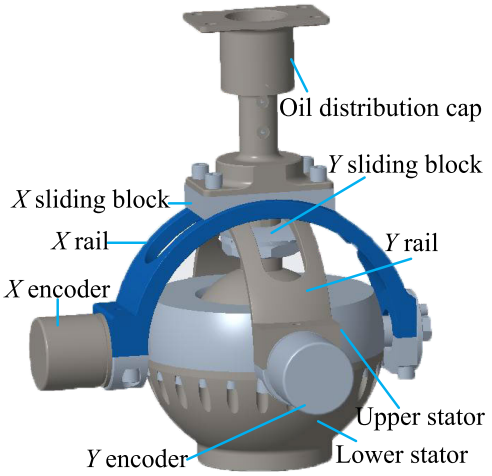

FIGURE 1. CAD model of the SMM.

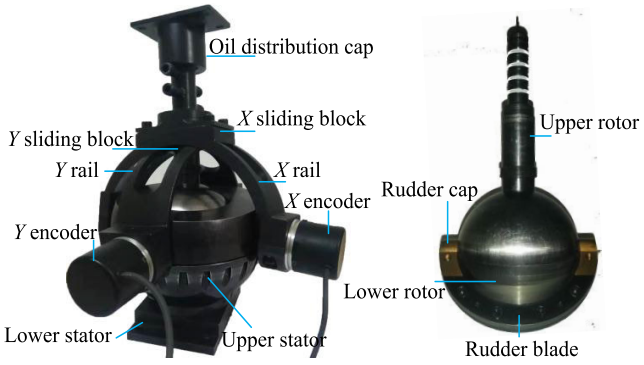

FIGURE 2. Prototype of the SMM.

For the sake of analysis, the following right-hand orthogonal reference coordinate frames are defined, as shown in Fig. 5.

- A fixed O-$X_0Y_0Z_0$ right-hand orthonormal reference coordinate frame is located at the stator, and the point O is the rotation center. X_0 and Y_0 are collinear with the rotation axis of the X and Y rails, respectively.
- A moving O-$X_1Y_1Z_1$ right-hand orthonormal reference coordinate frame is attached to the rudder blade with Z_1 and X_1 along the axis of the rudder blade and the central axis of the rudder cap, respectively.
- A moving O-xyz right-hand orthonormal reference coordinate frame is attached to the rotor with x along the X_0 axis and z along the axis of the rotor.
- An auxiliary O-UVW right-hand orthonormal reference coordinate frame represents the final orientation of the rotor.

  Furthermore, it is assumed that the established reference coordinate frames O-$X_0Y_0Z_0$, O-$X_1Y_1Z_1$, and O-xyz have the same orientation in the initial state.

There are two stators (upper and lower stators) and two rotors (upper and lower rotors). The upper and lower rotors as well as the upper and lower stators are connected through

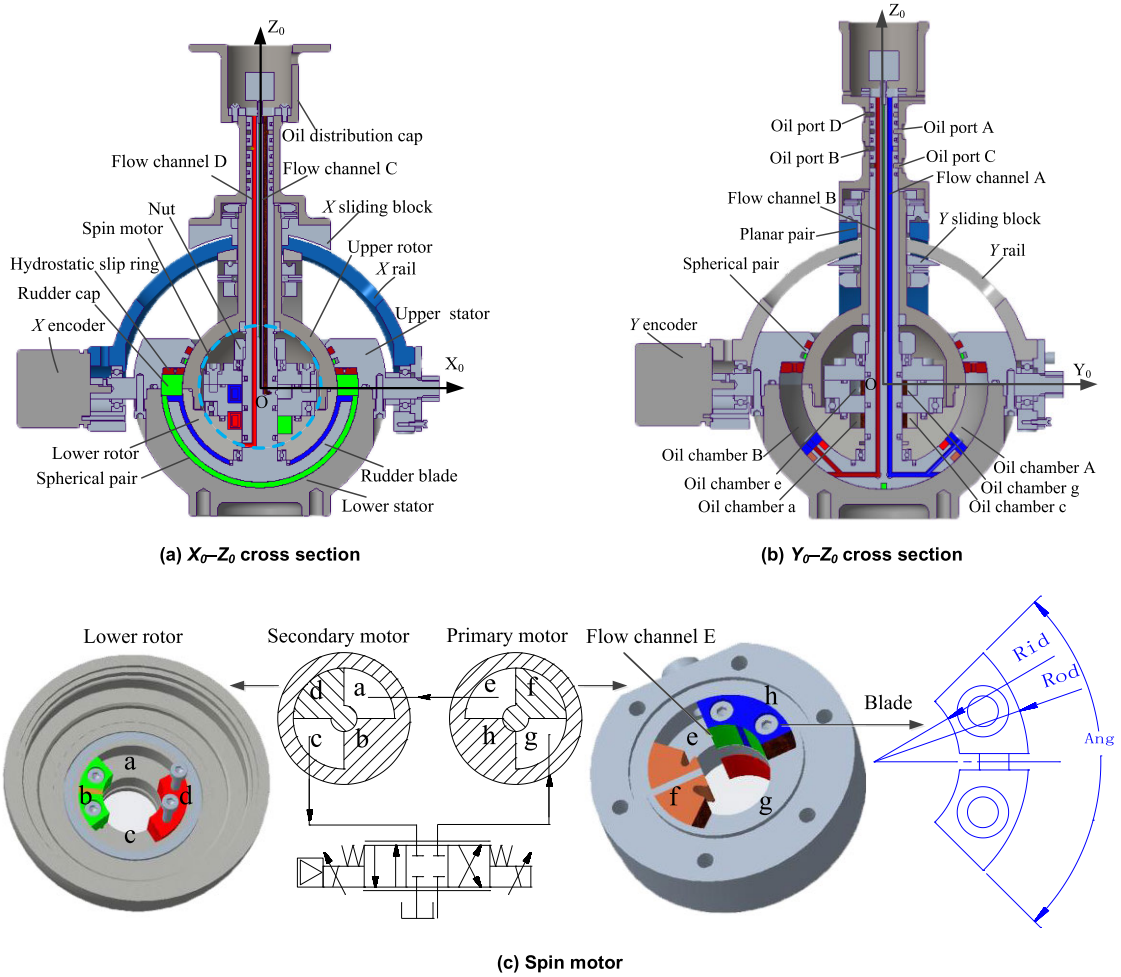

FIGURE 3. Architecture of the SMM.

screw threads. All spherical parts of the SMM are concentric. The rudder blade, which is supported concentrically by the lower stator via a spherical pair, can rotate around the X_1 axis. The clearance between the rudder blade and the lower stator is filled with hydraulic oil. The shafts of the rotor and the rudder blade are coaxial. The lower rotor, which is supported concentrically by the rudder blade via another spherical pair, can tilt with the rudder blade and rotate around the z axis relative to the rudder blade. The upper rotor is in contact with the upper stator via a spherical pair, allowing the rotor to rotate around the point O.

The orientation of the rotor relative to the stator can be measured via the measurement system. The measurement system consists of two arc-shaped rails (the X and Y rails), two sliding blocks (the X and Y sliding blocks), and two encoders (the X and Y encoders), as shown in Fig. 1. The X and Y rails mounted on the upper stator via four ball bearings are placed perpendicular to each other so that they can spin freely around the X_0 and Y_0 axes. The rotation angles of the rails relative to the fixed reference coordinate frame are measured by the X and Y encoders. Therefore, the orientation of the moving coordinate frame relative to the stator can be determined by the encoder readings. In addition, any external force acting on the rotor through its center of gravity must be supported by the reaction forces via the X rail, the Y rail, and ball bearings. In other words, the X and Y rails must also bear the external force exerted on the rotor. The external torque can be balanced by the output torque of the hydraulic system.

The rudder blade is shown in Fig. 4. The rudder cap is cylindrical and its axis passes through the spherical center. Support belts A and B play the important role of providing auxiliary support. The SMM has four independent flow channels: A, B, C and D. All these channels are arranged on the rudder blade, as shown in Fig. 3(a) and (b).

The hydraulic actuator consists of a swing hydraulic motor that actuates the rudder blade, a rotor to tilt an angle β around the X_1 axis, and a spin hydraulic motor that drives the rotor to spin an angle α around the z axis relative to the rudder blade.

The stator, the rotor, and the rudder blade form two closed oil chambers A and B, which are the working chambers of the swing hydraulic motor. To seal the two oil chambers, seal rings A and B are set between the lower rotor and the rudder

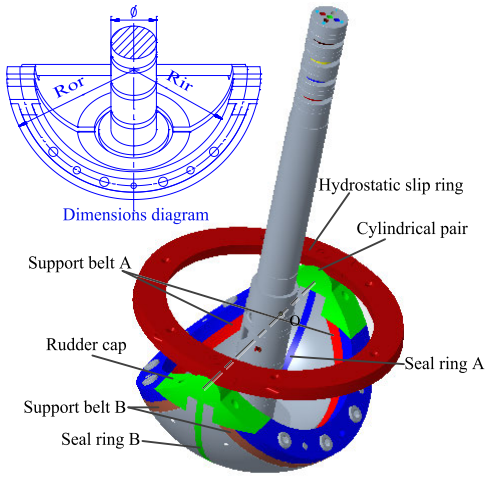

FIGURE 4. Rudder blade.

blade and between the lower stator and the rudder blade, as shown in Fig. 4. Thus, the swing hydraulic motor consists of oil chambers A and B, flow channels A and B, and oil ports A and B, as shown in Fig. 3(b). The working principle of the swing hydraulic motor is that the rudder blade and the rotor tilt an angle β around the X_1 axis when the pressure in oil chamber A is not equal to that in oil chamber B.

The spin hydraulic motor, mounted on the shaft of the rudder blade via a nut and ball bearings, comprises a primary motor and a secondary motor. The spin hydraulic motor is an ultra-full-cycle hydraulic motor that can rotate more than 360°, as shown in Fig. 3(a) and (c). In Fig. 3(c), a, c, e, and g represent the oil chambers and b, d, f, and h represent blades. The oil chambers a and e are connected to each other through the flow channel E. Consequently, different hydraulic pressure drops can induce different driving torques and actuate the rotor to achieve the desired equilibrium orientation.

There are two critical mechanical constraints.

Constraint 1: The hydrostatic slip ring is supported by the rudder cap via a cylindrical pair, as shown in Fig. 4. The hydrostatic slip ring is restricted to the X_0Y_0 plane by the upper stator, and hence, it has only one degree of freedom (i.e., rotation around the Z_0 axis).

Constraint 2: The X sliding block is fixed on the rotor. There is a planar pair between the X sliding block and the X rail, as shown in Fig. 3(b). Therefore, the rotor does not spin around the z axis relative to the X rail. However, the rotor can rotate around the z axis relative to the Y rail.

According to the above analysis, the orientation of the rotor can be determined by three rotations in order:

- The rotor tilts an angle β around the X_1 axis.
- The rotor spins an angle α around the z axis relative to the rudder blade.
- Due to *Constraint 1*, the rotor spins an angle θ about the Z_0 axis at the same time as it spins an angle α around the z axis relative to the rudder blade

Therefore, the SMM has two degrees of freedom: tilting an angle β around the X_1 axis and spinning an angle θ around the Z_0 axis.The main geometric parameters of the SMM are listed in Table 1.

TABLE 1. Geometric parameters of the SMM.

Symbol	Quantity	Value
R_{ir}	Inner radius of rudder blade	55(mm)
R_{or}	Outer radius of rudder blade	70(mm)
ϕ	Shaft diameter of rudder blade	25(mm)
R_{id}	Inner radius of blade	12.5(mm)
R_{od}	Outer radius of blade	22.5(mm)
Ang	Field angle of blade	89°
β	Tilt angle around the X_1 axis	[−0.25π,0.25π]
θ	Spin angle around the Z_0 axis	[0,2π]
α	Torsion angle around the z axis	[0,2π]

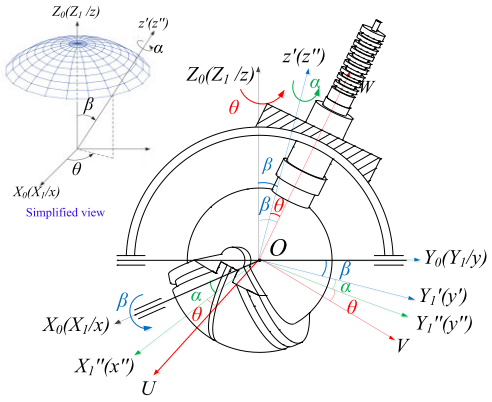

FIGURE 5. Orientation representation of the tilt– torsion– spin angles.

III. KINEMATICS

In this section, the forward kinematics of the SMM is presented by virtue of Euler transformation. The orientation of the SMM is illustrated by an intuitive representation of the tilt–torsion–spin $(\beta, -\alpha, \theta)$ angles, as shown in Fig. 5. K' and K'' represent the coordinate axes in the process of coordinate transformation.

Because only the rotation angles of the X and Y rails, θ_x, and θ_y, can be measured, the relationships among the angles α, β, θ, θ_x, and θ_y are required for carrying out the analysis. In general, three rotations taken about fixed axes yield the same final orientation as three rotations taken about the axes of the moving frame. Thus, the relationships among all above mentioned angles can be derived by the equivalent Euler transformation with respect to the coordinate frames *O-xyz* and *O-yxz*.

Based on homogeneous transformation, the orientation transformation matrix of the rotor about the X_0zZ_0 conversions can be formulated using Euler angles β, $-\alpha$, and θ.

$$\begin{aligned}\mathbf{T} &= \mathbf{R}_{X_0zZ_0}(\beta,-\alpha,\theta) = \mathbf{R}_{Z_0}(\theta)\mathbf{R}_{X_0}(\beta)\mathbf{R}_z(-\alpha)\\ &= \begin{bmatrix} C\alpha C\theta + S\alpha C\beta S\theta & S\alpha C\theta - C\alpha C\beta S\theta & S\beta S\theta \\ C\alpha S\theta - S\alpha C\beta C\theta & S\alpha S\theta + C\alpha C\beta C\theta & -S\beta C\theta \\ -S\alpha S\beta & C\alpha S\beta & C\beta \end{bmatrix}\end{aligned} \tag{1}$$

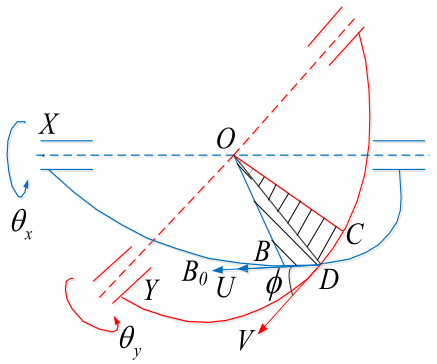

FIGURE 6. Illustration of the *X* and *Y* rails.

where C = cosine and S = sine. $\mathbf{R}_k(\omega)$ denotes a transformation matrix when an angle ω is spun about the k axis.

Fig. 6 shows the parameters employed in the derivation of the kinematic equations. B and C are the intermediate points of the X and Y rails, respectively. D is the intersection of the X and Y rails. The lines U and V intersecting at point D are tangential to the X and Y rails, respectively. The first Euler transformation matrix can be formulated using Euler angles θ_x, ψ_y, and ψ_z satisfying the xyz conversions (2), shown at the bottom of the next page.

where θ_x is the tilt angle of the X rail, $\psi_y = \angle BOD$, and ψ_z is the rotation angle of the rotor around the z axis relative to the X rail, $\psi_z = \angle BDB_0$.

The second Euler transformation matrix can be written using Euler angles θ_y, ξ_x, and ξ_y satisfying the yxz conversions:

$$\begin{aligned}&\mathbf{T}_2\\&= \mathbf{R}_y(\theta_y)\mathbf{R}_x(\xi_x)\mathbf{R}_z(\xi_z)\\&= \begin{bmatrix} S\theta_y S\xi_x S\xi_z + C\theta_y C\xi_z & S\theta_y S\xi_x C\xi_z - C\theta_y S\xi_z & S\theta_y C\xi_x \\ C\xi_x S\xi_z & C\xi_x C\xi_z & -S\xi_x \\ C\theta_y S\xi_x S\xi_z - S\theta_y C\xi_z & C\theta_y S\xi_x C\xi_z + S\theta_y S\xi_z & C\theta_y C\xi_x \end{bmatrix}\end{aligned} \tag{3}$$

where θ_y is the tilt angle of the Y rail, $\xi_x = \angle COD$, and ξ_z is the rotation angle of the rotor around the z axis relative to the Y rail, $\xi_z = \pi/2 - \phi$, where ϕ is the angle between the line U and V.

Solving equations (1) = (2) and (1) = (3), respectively, the following relations can be obtained as

$$\tan\theta_x = \tan\beta C\theta \tag{4}$$

$$\tan\theta_y = \tan\beta S\theta \tag{5}$$

$$\tan\theta = \tan\alpha / C\beta \tag{6}$$

Equations (4)–(6) indicate the relationships among rotation angles of the X rail, the Y rail, the rudder blade, and the rotor.

IV. PERFORMANCE OF THE MOTION MECHANISM

A. WORKSPACE

In this section, the workspace of the SMM is calculated in the Cartesian space. It should be noted that $0 \le \theta \le 2\pi$. The position vector of the end effector can be defined as

$$\begin{aligned}\mathbf{P} &= \mathbf{T}\begin{bmatrix}0 & 0 & L_z\end{bmatrix}^T\\&= L_z\begin{bmatrix}S\beta S\theta & -S\beta C\theta & C\beta\end{bmatrix}^T\end{aligned} \tag{7}$$

where $[0\ 0\ L_z]$ denotes the initial position of the end effector initial position, and L_z is the distance between the end effector and rotation center O.

As shown in Fig. 7, the workspace of the SMM is a part of a sphere whose radius is L_z. Moreover, the end effector of the SMM can tilt up to ±45°, which is determined by β, and can spin 360°, which is determined by θ.

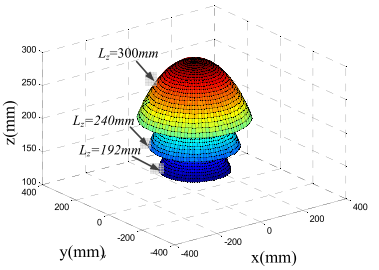

(a) Workspace with $-0.25\pi \le \beta \le 0.25\pi$

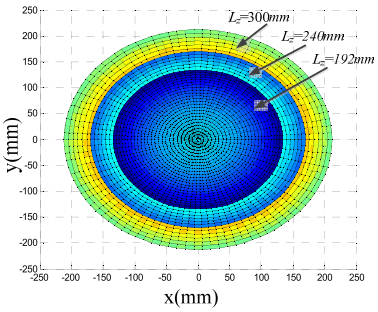

(b) *x–y* cross section

FIGURE 7. Workspace of the SMM.

B. DEXTERITY

The relationship between the angular velocity of the end effector and that of the driving joint of the SMM can be expressed using the Jacobian matrix.

$$\boldsymbol{\omega}_r = \mathbf{J}\dot{\boldsymbol{\vartheta}} \tag{8}$$

where $\dot{\boldsymbol{\vartheta}} = [\dot{\beta}\ \dot{\theta}]^T$, $\mathbf{J}$ is the Jacobian matrix, ω_r represents the angular velocity of the rotor under the coordinate system O-$X_0Y_0Z_0$.

$$\begin{aligned}\boldsymbol{\omega}_r &= \begin{bmatrix}\omega_{r.x} & \omega_{r.y} & \omega_{r.z}\end{bmatrix}^T\\&= \begin{bmatrix}C\theta & -S\beta S\theta & 0\\ S\theta & S\beta C\theta & 0\\ 0 & -C\beta & 1\end{bmatrix}\begin{bmatrix}\dot{\beta}\\ \dot{\alpha}\\ \dot{\theta}\end{bmatrix}\end{aligned} \tag{9}$$

Taking the inverse tangent of (6), α can be expressed as

$$\alpha = \arctan(\tan\theta C\beta) \tag{10}$$

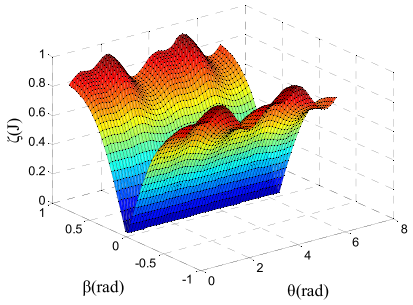

FIGURE 8. Performance index.

Differentiating (10) with respect to time yields (11)

$$\dot{\alpha} = \frac{\left(C\beta \sec^2\theta\right)\dot{\theta} - (\tan\theta S\beta)\,\dot{\beta}}{1 + \tan^2\theta C^2\beta} \tag{11}$$

Substituting (11) into (9), the Jacobian matrix can be written as

$$\mathbf{J} = \begin{bmatrix} C\theta + \dfrac{\tan\theta S\theta S^2\beta}{1+\tan^2\theta C^2\beta} & -\dfrac{S\theta S\beta C\beta \sec^2\theta}{1+\tan^2\theta C^2\beta} \\ S\theta - \dfrac{C\theta S^2\beta}{1+\tan^2\theta C^2\beta} & \dfrac{S\beta C\beta \sec\theta}{1+\tan^2\theta C^2\beta} \\ \dfrac{\tan\theta S\beta C\beta}{1+\tan^2\theta C^2\beta} & 1 - \dfrac{C^2\beta \sec^2\theta}{1+\tan^2\theta C^2\beta} \end{bmatrix} \tag{12}$$

To obtain better insight into the singularities and dexterity performance of the SMM, the condition number is calculated. The condition number of a dimensionally homogeneous Jacobian matrix is defined as

$$\kappa(\mathbf{J}) = \|\mathbf{J}\| \left\|\mathbf{J}^{-1}\right\| \tag{13}$$

with

$$\|\mathbf{J}\| = \sqrt{\frac{1}{n}\mathrm{tr}(\mathbf{J}^T\mathbf{J})}$$
$$\left\|\mathbf{J}^{-1}\right\| = \sqrt{\frac{1}{n}\mathrm{tr}[(\mathbf{J}^T\mathbf{J})^{-1}]}$$

where $||\mathbf{J}||$ is the weighted Frobenius norm of $\mathbf{J}$ with $n = 2$ as weight. $\kappa(\mathbf{J})$ can have values from unity to infinity, and for that reason the performance index $\zeta(\mathbf{J})$, given by its inverse, is employed. $\zeta(\mathbf{J}) \approx 0$ denotes a singular pose, whereas $\zeta(\mathbf{J}) = 1$ denotes an isotropic pose.

Fig. 8 shows $\zeta(\mathbf{J})$ against the actuated rotations. It can be estimated that approximately 10% of points reached in the theoretical workspace given $\zeta(\mathbf{J}) \leq 0.25$, indicating behavior far from isotropy. Approximately 75% of points have $\zeta(\mathbf{J}) > 0.75$, indicating behavior close to isotropy.

Therefore, the singular pose is reached whenever $\beta = 0$. In that case, the $Z_1(z)$ axis coincides with the Z_0 axis. Even if the rudder blade spins about the Z_1 axis, the position of the end effector remains unchanged.

V. DYNAMICS

In this section, for designing the controller, the dynamic model of the SMM is determined systematically based on Lagrange's equations. The entire system can be divided into three parts: rudder blade, rotor, and spin motor. The modeling process includes selecting the generalized coordinates, formulating the kinetic and potential energy, and calculating Lagrange's equations.

A. CHOICE OF GENERALIZED COORDINATES

Because the dynamics modeling is based on rigid body dynamics and employs hydraulic transmission, the following two assumptions are made:

Assumption 1: Ignoring the elastic effects of the system, all parts of the SMM are regarded as rigid bodies.

Assumption 2: Ignore the viscosity damping force/torque when sharing the oil film between faces.

According to the above working principle analysis, $\mathbf{q} = [\alpha\ \beta]^T$ can be selected as the generalized coordinates. For the SMM, α and β denote the rotation angles around the z and X_1 axes, respectively.

B. KINETIC ENERGY

The total kinetic energy is the sum of the kinetic energies of the rudder blade, rotor, and spin hydraulic motor. The SMM has only rotational motion. Thus, the kinetic energy of the SMM is composed of only rotational kinetic energy. Therefore, the total kinetic energy can be expressed as

$$K = K_b + K_r + K_m \tag{14}$$

where K_b, K_r, and K_m denote the kinetic energies of the rudder blade, rotor, and spin motor, respectively.

$$K_i = \frac{1}{2}\boldsymbol{\omega}_i^T \mathbf{I}_i \boldsymbol{\omega}_i, \quad i = b, r, m \tag{15}$$

where ω_i and I_i denote the angular velocity and inertia moment, respectively. The subscripts b, r, and m denote the rudder blade, rotor, and spin hydraulic motor, respectively.

Based on the theory of fixed-point rotation, the angular velocity of the rudder blade, $\boldsymbol{\omega}_b$, can be expressed as

$$\boldsymbol{\omega}_b = [\,\dot{\beta} \quad \dot{\theta}S\beta \quad \dot{\theta}C\beta\,]^T \tag{16}$$

$$\mathbf{T}_1 = \mathbf{R}_x(\theta_x)\mathbf{R}_y(\psi_y)\mathbf{R}_z(\psi_z) = \begin{bmatrix} C\psi_y C\psi_z & -C\psi_y S\psi_z & S\psi_y \\ C\psi_z S\theta_x S\psi_y + S\psi_z C\theta_x & C\theta_x C\psi_z - S\theta_x S\psi_y S\psi_z & -S\theta_x C\psi_y \\ S\theta_x S\psi_z - C\theta_x S\psi_y C\psi_z & C\psi_z S\theta_x + C\theta_x S\psi_y S\psi_z & C\theta_x C\psi_y \end{bmatrix} \tag{2}$$

The rotation angle of the rotor around the z axis is $-\alpha$. Thus, the angular velocity of the rotor, $\boldsymbol{\omega}_r$, can be written as

$$\boldsymbol{\omega}_r = \begin{bmatrix} \dot{\theta}S\beta S(-\alpha) + \dot{\beta}C(-\alpha) \\ \dot{\theta}S\beta C(-\alpha) - \dot{\beta}S(-\alpha) \\ \dot{\theta}C\beta + (-\dot{\alpha}) \end{bmatrix} \tag{17}$$

Owing to its two-stage structure, the spin hydraulic motor rotates an angle $-\alpha/2$ around the z axis. Therefore, the angular velocity of the spin hydraulic motor, $\boldsymbol{\omega}_m$, can be obtained as

$$\boldsymbol{\omega}_m = \begin{bmatrix} \dot{\theta}S\beta S(-\alpha/2) + \dot{\beta}C(-\alpha/2) \\ \dot{\theta}S\beta C(-\alpha/2) - \dot{\beta}S(-\alpha/2) \\ \dot{\theta}C\beta + (-\dot{\alpha}/2) \end{bmatrix} \tag{18}$$

$$\mathbf{I}_i = \mathrm{diag}(\, I_{i.xx} \quad I_{i.yy} \quad I_{i.zz}\,) \tag{19}$$

where $I_{i.xx}$, $I_{i.yy}$, and $I_{i.zz}$ denote the inertia moment with respect to the X_i, Y_i, and Z_i axes in the self-coordinate system, respectively. Because of axial symmetry, $I_{i.xx} = I_{i.yy} \neq I_{i.zz}$.

C. POTENTIAL ENERGY

The total potential energy is the sum of the potential energies of the rudder blade, rotor, and spin hydraulic motor. To simplify the analysis, assume the X_0Y_0 plane has zero potential energy.

The potential energy of the rudder blade, P_b, can be given as

$$P_b = m_b g l_{b0} C\beta \tag{20}$$

The potential energy of the rotor, P_r, can be expressed as

$$P_r = m_r g l_{r0} C\beta \tag{21}$$

The potential energy of the spin hydraulic motor, P_m, can be obtained as

$$P_m = m_m g l_{m0} C\beta \tag{22}$$

where m_i denotes mass, and l_{i0} is the distance from the center of gravity to the rotation center.

Therefore, the entire potential energy of the SMM P can be formulated as

$$P = P_b + P_r + P_m \tag{23}$$

D. DYNAMIC EQUATIONS

Lagrange's equations can be expressed as:

$$L = \sum_{i=1}^{n} K_i - \sum_{i=1}^{n} P_i \tag{24}$$

$$\tau_q = \frac{d}{dt}\frac{\partial L}{\partial \dot{q}} - \frac{\partial L}{\partial q} \tag{25}$$

where L is the Lagrange function, and τ_q denotes the generalized force or torque vector in the generalized coordinate system.

Based on the foregoing analysis, the dynamic characteristic of the SMM can be formulated as

$$\mathbf{M}(\mathbf{q})\ddot{\mathbf{q}} + \mathbf{C}(\mathbf{q}, \dot{\mathbf{q}})\dot{\mathbf{q}} + \mathbf{G}(\mathbf{q}) = \tau \tag{26}$$

where $\mathbf{M}(\mathbf{q})$ is the inertia matrix, $\mathbf{C}(\mathbf{q}, \dot{\mathbf{q}})$ denotes the combined centripetal and Coriolis torque vector, $\mathbf{G}(\mathbf{q})$ is the gravitational torque vector, and τ represents the equivalent generalized torque vector applied on the rotor in the generalized coordinate system. The centripetal and Coriolis torque can be ignored in low-speed motion. The explicit expressions of the terms in (26) are given in the appendix.

VI. RBFSMC DESIGN

From the dynamics analysis, it can be observed that the system of the SMM exhibits highly nonlinear and multivariable characteristics. The dynamic model is determined after some reasonable simplifications. Because SMC does not depend on a perfect mathematical model and is robust against external disturbances and model uncertainties, select the RBFSMC to track the desired trajectory accurately.

A. SELECTION OF THE SLIDING SURFACE

Considering the external disturbance, the dynamic model can be expressed as

$$\mathbf{M}(\mathbf{q})\ddot{\mathbf{q}} + \mathbf{C}(\mathbf{q}, \dot{\mathbf{q}})\dot{\mathbf{q}} + \mathbf{G}(\mathbf{q}) + \tau_d = \tau \tag{27}$$

where τ_d denotes the external disturbance, including friction, and neglected nonlinear terms.

The tracking errors can be defined as

$$\mathbf{e} = \mathbf{q}_d - \mathbf{q} \tag{28}$$

where $\mathbf{q}_d$ and $\mathbf{q}$ represent the desired and actual position trajectories, respectively.

Next, choose the sliding surface function as

$$\mathbf{R} = \mathbf{K}_d\dot{\mathbf{e}} + K_p\mathbf{e} \tag{29}$$

where $\mathbf{K}_d = \mathrm{diag}(\lambda_{d1}, \lambda_{d2})$ and $\mathbf{K}_p = \mathrm{diag}(\lambda_{p_1}, \lambda_{p_2})$ are positive definite constant matrices, $\dot{\mathbf{e}} = \dot{\mathbf{q}}_d - \dot{\mathbf{q}}$.

B. LYAPUNOV FUNCTION DEFINITION

After selection of the sliding surface, the Lyapunov function for SMC is defined.

Combining (27), (28), and (29), the following equations are obtained as

$$\dot{\mathbf{q}} = \dot{\mathbf{q}}_d - \mathbf{K}_d^{-1}\mathbf{R} + \mathbf{K}_d^{-1}\mathbf{K}_p\mathbf{e} \tag{30}$$

$$\begin{aligned} \mathbf{M}\mathbf{K}_d^{-1}\dot{\mathbf{R}} &= \mathbf{M}\mathbf{K}_d^{-1}[\mathbf{K}_d\ddot{\mathbf{q}}_d + \mathbf{K}_p\dot{\mathbf{e}} - \mathbf{K}_d\ddot{\mathbf{q}}] \\ &= \mathbf{M}(\ddot{\mathbf{q}}_d + \mathbf{K}_d^{-1}\mathbf{K}_p\dot{\mathbf{e}}) + \mathbf{C}(\dot{\mathbf{q}}_d + \mathbf{K}_d^{-1}\mathbf{K}_p\mathbf{e}) \\ &\quad + \mathbf{G} - \mathbf{C}\mathbf{K}_d^{-1}\mathbf{R} + \tau_d - \tau \end{aligned} \tag{31}$$

with

$$\mathbf{f}(\mathbf{x}) = \mathbf{M}(\ddot{\mathbf{q}}_d + \mathbf{K}_d^{-1}\mathbf{K}_p\dot{\mathbf{e}}) + \mathbf{C}(\dot{\mathbf{q}}_d + \mathbf{K}_d^{-1}\mathbf{K}_p\mathbf{e}) + \mathbf{G} \tag{32}$$

where $\mathbf{x} = [\mathbf{e}, \dot{\mathbf{e}}, \mathbf{q}_d, \dot{\mathbf{q}}_d, \ddot{\mathbf{q}}_d]^T$ is the system input. $\mathbf{f}(\mathbf{x})$denotes the uncertain term.

The approximate control law can be designed as

$$\tau = \hat{\mathbf{f}}(\mathbf{x}) + \mathbf{K}_v\mathbf{R} \tag{33}$$

where $\hat{\mathbf{f}}(x)$ denotes an estimation of $\mathbf{f}(\mathbf{x})$ used RBFNN, and $\mathbf{K}_v = \mathrm{diag}(\lambda_{v_1}, \lambda_{v_2})$ is a positive definite constant matrix.

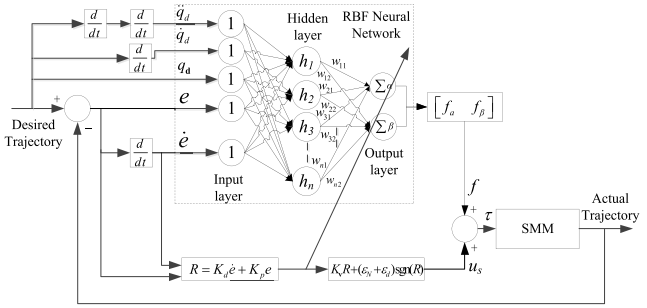

FIGURE 9. Block diagram of the RBFSMC.

Substituting (32) and (33) into (31), (31) can then be rewritten as

$$\mathbf{M}\mathbf{K}_d^{-1}\dot{\mathbf{R}} = (\mathbf{f} - \hat{\mathbf{f}}) - (\mathbf{C}\mathbf{K}_d^{-1} + \mathbf{K}_v)\mathbf{R} + \tau_d \tag{34}$$

The Lyapunov function can be defined as

$$L = \frac{1}{2}\mathbf{R}^T\mathbf{M}\mathbf{K}_d^{-1}\mathbf{R} \tag{35}$$

Differentiating (35) with respect to time yields (36)

$$\begin{aligned}\dot{L} &= \mathbf{R}^T\mathbf{M}\mathbf{K}_d^{-1}\dot{\mathbf{R}} + \frac{1}{2}\mathbf{R}^T\dot{\mathbf{M}}\mathbf{K}_d^{-1}\mathbf{R} \\ &= \frac{1}{2}\mathbf{R}^T(\dot{\mathbf{M}}\mathbf{K}_d^{-1} - 2\mathbf{C}\mathbf{K}_d^{-1} - 2\mathbf{K}_v)\mathbf{R} + \mathbf{R}^T(\mathbf{f} - \hat{\mathbf{f}} + \tau_d)\end{aligned} \tag{36}$$

It can be seen that the stability of the control system mainly depends on $\mathbf{f} - \hat{\mathbf{f}} + \tau_d$, that is, the approximate error $\mathbf{f} - \hat{\mathbf{f}}$ and the interference term τ_d. For this reason, the RBFNN is employed to approximate $\mathbf{f}$.

C. RBFNN AND STABILITY ANALYSIS

1) STRUCTURE OF RBFNN

To improve the stability of the system, utilize the RBFNN to estimate the uncertain term $\mathbf{f}$. The block diagram of the RBFSMC is shown in Fig. 9.

The structure of the RBFNN is as follows:

- The input layer: $\mathbf{x} = [\mathbf{e}, \dot{\mathbf{e}}, \mathbf{q}_d, \dot{\mathbf{q}}_d, \ddot{\mathbf{q}}_d]^T$ is a vector of five inputs to the network.
- The hidden layer: $\boldsymbol{\delta} = [\delta_1, \delta_2 \ldots, \delta_n]^T$ is a vector of n activation functions of RBFNN. The activation functions of RBFNN based on Gaussian function [28] can be expressed as

$$\delta_j = \sum_{j=1}^{n} \phi(\|x - c_j\|^2) = e^{-\frac{\|x - c_j\|^2}{2\sigma_j^2}} \tag{37}$$

where c_j and σ_j denote the center vector of the *jth* hidden network node and standard constant of RBFNN, respectively.

- The output layer: The output value can be written as

$$\mathbf{f} = w_j \sum_{j=1}^{n} \phi(\|x - c_j\|^2) = \mathbf{W}^T\boldsymbol{\delta} \tag{38}$$

where $\mathbf{W} = [w_{11}, w_{21}, \ldots, w_{n1}; w_{12}, w_{22}, \ldots, w_{n2}]^T$ denotes the ideal network weight vector that connects the hidden layer and the output layer.

2) TRAINING AND CENTER PLACEMENT IN AN RBFNN

Generally, the training procedure for RBFNN is divided into two stages: an unsupervised training for the center adjustment of the activation functions in the hidden layer, followed by a supervised training for the weight adjustment between the output layer and the hidden layer. In this study, the centers of the activation functions are adjusted by the k-mean algorithm.

3) THE K-MEAN ALGORITHM FOR CENTER ADJUSTMENT

The k-means algorithm is an unsupervised method for data clustering. It divides the input space into k classes, as follows:

- Choose a number of classes ($k = 5$ is the number of inputs to the RBFNN).
- Initialize the centers of the activation functions ($c_j(0)$ and $\beta(0)$)
- Compute the Euclidean distance between the center of each activation function and the input vector $\mathbf{X}$

$$d_j(t) = \| x(t) - c_j(t-1) \|, \quad (j = 1, 2, \cdots, a) \tag{39}$$

$$c_r = \{c_j, d_r = \min\{d_j(t)\}\} \tag{40}$$

- Adjust the vector of centers using the following adaption law.

$$c_r(t) = c_r(t-1) + \beta(t)[x(t) - c_r(t-1)] \tag{41}$$

- Update the learning rate using the following adaption law.

$$\beta(t) = \beta(t-1)\Big/\sqrt{1 + \text{int}(t/a)} \tag{42}$$

where t is the time, a is the number of the hidden nodes, $\text{int}(t/a)$ is the integer part of t/a, $\beta(t)$ represents the learning rate and $0 \le \beta(t) \le 1$, and r denotes the sequence number of the hidden node when the distance between $x(t)$ and $c_j(t-1)$ is minimum.

When $\beta(t) \to 0$, stop the iteration and obtain the values of c_j.

4) STABILITY ANALYSIS AND WEIGHT ADAPTION

The network weights are updated by the decreasing gradient method so that the final output of the RBFNN gradually approximates the sliding mode equivalent control along the sliding surface in which the sliding mode state is asymptotically stable. The RBFNN adaption output can be expressed as

$$\hat{\mathbf{f}} = \hat{\mathbf{W}}^T\boldsymbol{\delta}(x) \tag{43}$$

$$\mathbf{f} - \hat{\mathbf{f}} = \tilde{\mathbf{W}}^T\boldsymbol{\delta}(\mathbf{x}) + \varepsilon \tag{44}$$

where $\tilde{\mathbf{W}} = \mathbf{W} - \hat{\mathbf{W}}$, $\hat{\mathbf{W}}$ is the RBFNN adaptation law, and $\boldsymbol{\varepsilon}$ denotes an approximate error.

Substituting (43) into (33), the approximate control law can be derived as

$$\tau = \hat{\mathbf{W}}^T\boldsymbol{\delta}(\mathbf{x}) + \mathbf{K}_v\mathbf{R} - \mathbf{v} \tag{45}$$

$$\mathbf{v} = -(\varepsilon_N + \varepsilon_d)\text{sgn}(\mathbf{R}) \tag{46}$$

$$\text{sgn}(\mathbf{R}) = \begin{cases} 1 & if \ \ \mathbf{R} > 0 \\ -1 & if \ \ \mathbf{R} < 0 \end{cases} \tag{47}$$

where $\mathbf{v}$ is the robust term to overcome the approximate error and interference term $\boldsymbol{\tau}_d$, $||\boldsymbol{\varepsilon}|| \leq \varepsilon_N$, $||\boldsymbol{\tau}_d|| \leq \varepsilon_d$, ε_N and $\varepsilon_{\mathbf{d}}$ are robust coefficients.

Substituting (45) into (31), (31) can be rewritten as

$$\mathbf{M}\mathbf{K}_d^{-1}\dot{\mathbf{R}} = \tilde{\mathbf{W}}^T\boldsymbol{\delta}(\mathbf{x}) - (\mathbf{C}\mathbf{K}_d^{-1} + \mathbf{K}_v)\mathbf{R} + (\tau_d + \boldsymbol{\varepsilon}) + \mathbf{v} \quad (48)$$

To ensure the system is asymptotically stable, $\dot{L}$ must be negative. Therefore, the following function can be regarded as the RBFNN adaptation law.

$$\dot{\hat{\mathbf{W}}} = -\dot{\tilde{\mathbf{W}}} = \mathbf{K}_R\boldsymbol{\delta}\mathbf{R}^T \quad (49)$$

Thus, the network weight can be updated as follows:

$$\mathbf{W}(t) = \mathbf{W}(t-1) + \mathbf{K}_R\boldsymbol{\delta}\mathbf{R}^T \quad (50)$$

where $\mathbf{K}_R$ is a positive definite constant matrix.

The Lyapunov function can be redefined as

$$L = \frac{1}{2}\mathbf{R}^T\mathbf{M}\mathbf{K}_d^{-1}\mathbf{R} + \frac{1}{2}\mathrm{tr}(\tilde{\mathbf{W}}^T\mathbf{K}_R^{-1}\tilde{\mathbf{W}}) \quad (51)$$

Differentiating (51) with respect to time yields (52)

$$\begin{aligned}
\dot{L} &= \mathbf{R}^T\mathbf{M}\mathbf{K}_d^{-1}\dot{\mathbf{R}} + (\mathbf{R}^T\dot{\mathbf{M}}\mathbf{K}_d^{-1}\mathbf{R})\Big/2 + \mathrm{tr}(\tilde{\mathbf{W}}^T\mathbf{K}_R^{-1}\dot{\tilde{\mathbf{W}}}) \\
&= \mathbf{R}^T\tilde{\mathbf{W}}^T\boldsymbol{\delta}(\mathbf{x}) - \mathbf{R}^T(\mathbf{C}\mathbf{K}_d^{-1} + \mathbf{K}_v)\mathbf{R} + \mathbf{R}^T(\tau_d + \varepsilon + \mathbf{v}) \\
&\quad + (\mathbf{R}^T\dot{\mathbf{M}}\mathbf{K}_d^{-1}\mathbf{R})\Big/2 + \mathrm{tr}(\tilde{\mathbf{W}}^T\mathbf{K}_R^{-1}\dot{\tilde{\mathbf{W}}}) \\
&= [\mathbf{R}^T(\dot{\mathbf{M}} - 2\mathbf{C})\mathbf{K}_d^{-1}\mathbf{R}]\Big/2 - \mathbf{R}^T\mathbf{K}_v\mathbf{R} + \mathbf{R}^T(\tau_d + \varepsilon + \mathbf{v}) \\
&\quad + \mathbf{R}^T\tilde{\mathbf{W}}^T\boldsymbol{\delta}(\mathbf{x}) + \mathrm{tr}(\tilde{\mathbf{W}}^T\mathbf{K}_R^{-1}\dot{\tilde{\mathbf{W}}}) \\
&= [\mathbf{R}^T(\dot{\mathbf{M}} - 2\mathbf{C})\mathbf{K}_d^{-1}\mathbf{R}]\Big/2 - \mathbf{R}^T\mathbf{K}_v\mathbf{R} + \mathbf{R}^T(\tau_d + \varepsilon + \mathbf{v}) \\
&\quad + \mathrm{tr}\tilde{\mathbf{W}}^T[\mathbf{K}_R^{-1}\dot{\tilde{\mathbf{W}}} + \boldsymbol{\delta}\mathbf{R}^T] \\
&= -\mathbf{R}^T\mathbf{K}_v\mathbf{R} + \mathbf{R}^T(\tau_d + \varepsilon + \mathbf{v}) \quad (52)
\end{aligned}$$

Due to

$$\begin{aligned}
\mathbf{R}^T(\boldsymbol{\tau}_d + \boldsymbol{\varepsilon} + \mathbf{v}) &= \mathbf{R}^T(\boldsymbol{\tau}_d + \boldsymbol{\varepsilon}) + \mathbf{R}^T\mathbf{v} \\
&= \mathbf{R}^T(\boldsymbol{\tau}_d + \boldsymbol{\varepsilon}) - \left\|\mathbf{R}^T\right\|(\varepsilon_N + \varepsilon_d) \\
&\leq 0 \quad (53)
\end{aligned}$$

Therefore

$$\dot{L} \leq -\mathbf{R}^T\mathbf{K}_v\mathbf{R} \leq 0 \quad (54)$$

In summary, according to Lyapunov theory, the RBFSMC can ensure asymptotic stability of the control system. When $t \to \infty$, the following dynamic characteristic can be achieved

$$\mathbf{R} = \mathbf{K}_d\dot{\mathbf{e}} + \mathbf{K}_p\mathbf{e} = 0 \quad (55)$$

Consequently, the tracking error approaches zero along the sliding surface.

TABLE 2. Mass and inertia properties of the SMM.

Body	l_i(mm)	m_i(kg)	$\mathbf{I}_i$(kg.m^2)
Rubble blade	5.0	3.9	diag(0.027,0.027,0.005)
Spin motor	3.5	1.2	diag(0.01,0.01,0.001)
Rotor	3.0	5.4	diag(0.032,0.032,0.056)

VII. RESULTS

A. SIMULATION VERIFICATION

In this section, to validate the feasibility of the designed SMM and RBFSMC, some simulations are implemented using the MATLAB/Simulink. The mass and inertia properties of the SMM considered in the simulations are listed in Table 2.

In this study, the SMC is designed as follows:

The sliding surface function is defined as

$$\mathbf{R}_s = \mathbf{K}_{ds}\dot{\mathbf{e}} + \mathbf{K}_{ps}\mathbf{e} \quad (56)$$

The control rule is designed as

$$\tau_s = \mathbf{K}_{vs}\mathbf{R} + (\varepsilon_{Ns} + \varepsilon_{ds})\mathrm{sgn}(\mathbf{R}) \quad (57)$$

where $\mathbf{K}_{ds}$, $\mathbf{K}_{ps}$, and $\mathbf{K}_{vs}$ are positive definite constant matrices, ε_{Ns} and ε_{ds} are robust coefficients.

To comprehensively evaluate the control method, two cases are simulated.

Case 1: Choose step signal as input.

Case 2: Choose sinusoidal signal as input. Two piecewise functions are employed to simulate equivalent external disturbance.

Define the initial states $[\alpha\dot{\alpha}\beta\dot{\beta}] = [0000]$. The relevant controller parameters are listed in Table 3. The Gaussian parameters are as follows.

$$c = \begin{bmatrix} -2 & -1.5 & -1 & 0 & 1 & 1.5 & 2 \\ -2 & -1.5 & -1 & 0 & 1 & 1.5 & 2 \\ -2 & -1.5 & -1 & 0 & 1 & 1.5 & 2 \\ -2 & -1.5 & -1 & 0 & 1 & 1.5 & 2 \\ -2 & -1.5 & -1 & 0 & 1 & 1.5 & 2 \end{bmatrix},$$
$$\sigma_j = 0.2 \quad j = 1, 2, \ldots, 7$$

First, the step response is simulated to investigate the dynamic performance. The reference values of settling time and overshoot are 0.5 s and 5%, respectively. As seen in Figs. 10 and 11, the SMM with RBFSMC can rapidly reach the desired trajectory in the α and β directions respectively

TABLE 3. Relevant controller parameters.

Symbol	Value	Symbol	Value
$\mathbf{K}_p$	diag(5,5)	$\mathbf{K}_R$	diag(30,30,30,30,30,30,30)
$\mathbf{K}_d$	diag(2,2)	ε_N	0.5
$\mathbf{K}_v$	diag(48,48)	ε_d	0.2
$\beta(0)$	rand(5,1)	W_0	rand(7,2)
$\mathbf{K}_{ps}$	diag(8,8)	ε_{Ns}	0.8
$\mathbf{K}_{ds}$	diag(3,3)	ε_{ds}	1.0

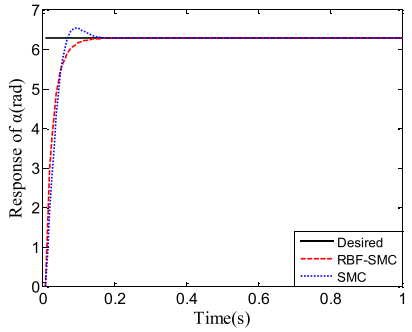

FIGURE 10. Step response in the α direction.

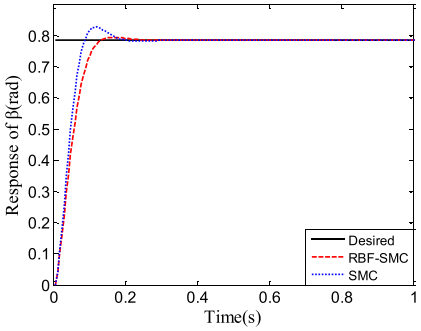

FIGURE 11. Step response in the β direction.

with a settling time of 0.1 s and 0.2 s, and an overshoot of 0 rad and 0.01 rad. Note that the system using the RBFSMC responds quickly and has only a small overshoot in the β direction. The SMM with SMC has the same settling time as RBFSMC. However, it has a large overshoot of 0.25 rad and 0.04 rad in the α and β directions, respectively.

Furthermore, to validate the universality of RBFSMC, the other desired trajectory is selected as

$$\mathbf{q} = [\, S(t/2) \quad \pi/4 S(t/2)\,], \quad L_z = 192mm \tag{58}$$

For demonstrating the robustness of the control method, two piecewise functions are employed to simulate the equivalent external disturbance:

$$\tau_d = \begin{cases} [0 \;\; 0] & t \le 5 \\ [2S(\pi t) \; 2S(\pi t)] & t > 5 \end{cases} \tag{59}$$

The trajectory tracking results and the corresponding torque inputs using the RBFSMC and SMC are given in Figs.12-15, respectively. The rotation angles of the X and Y rails using the RBFSMC and SMC are shown in Fig. 21(a) and (b), respectively. The reference value of tracking errors is 5%, i.e., 0.05 rad and 0.04 rad in the α and β directions, respectively.

As shown in Figs. 12 and 14, the RBFSMC gives a small error about 0.05 rad and 0.01 rad in the α and β directions respectively, while the SMC gives an error about 0.25 rad and 0.08 rad. Hence, the RBFSMC achieves higher tracking accuracy than the SMC.

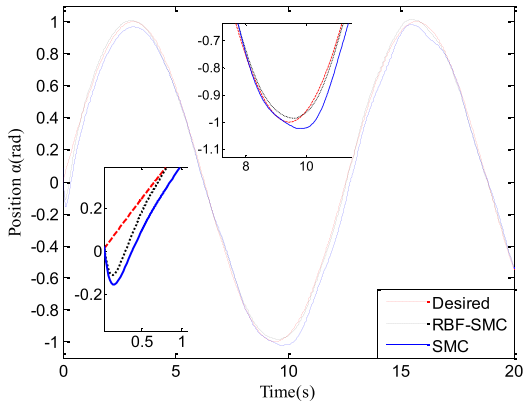

FIGURE 12. Trajectory tracking in the α direction.

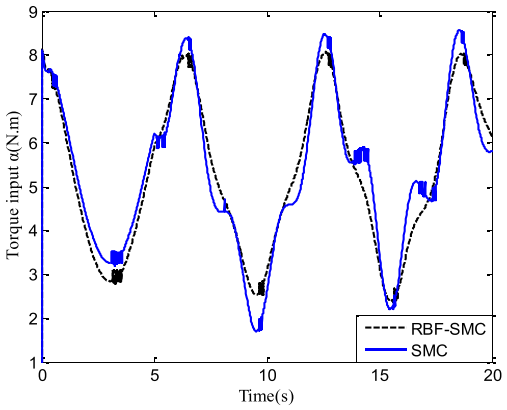

FIGURE 13. Torque input in the α direction.

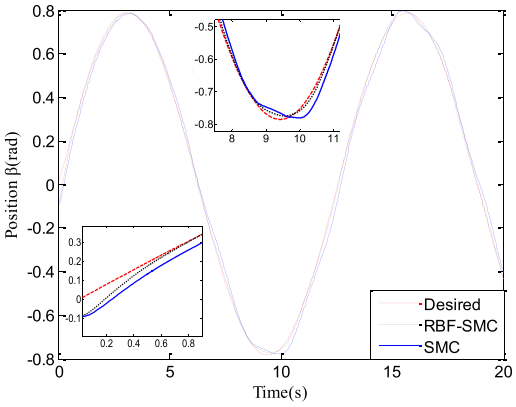

FIGURE 14. Trajectory tracking in the β direction.

At $T = 5$ s, the equivalent external disturbance is applied to the system. The torque inputs using the SMC are observed to give larger oscillations than before, especially in the β direction. Apparently, the fluctuation of torque inputs using the RBFSMC is smaller than that of the SMC, which shows strong robustness of the RBFSMC (Figs. 13 and 15).

Fig. 16 shows the approximating curve of RBFNN, which indicates that the RBFNN using a Gaussian function as the activation function has a good adaptive approximation performance.

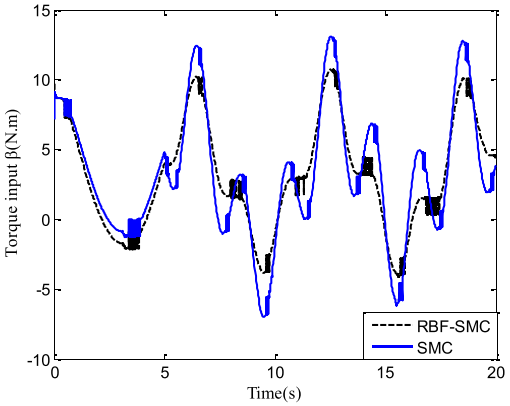

FIGURE 15. Torque input in the β direction.

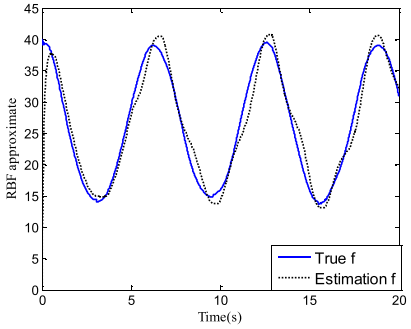

FIGURE 16. Approximation curve of RBFNN.

TABLE 4. Parameters of main parts.

Parts	Quantity	Value
Pump	Displacement(ml/rev)	25
	Speed(rev/min)	1500
	Nominal pressure(MPa)	31.5
Motor	Power(kW)	11
Servo valve	Nominal flow with Δp 10 bar P-T(L/min)	26
	Reference Rising response time(ms)	50
	time±100% Fall response time(ms)	25
Encoder	Maximum response frequency(kHz)	200
	Slewing speed(r/min)	12000

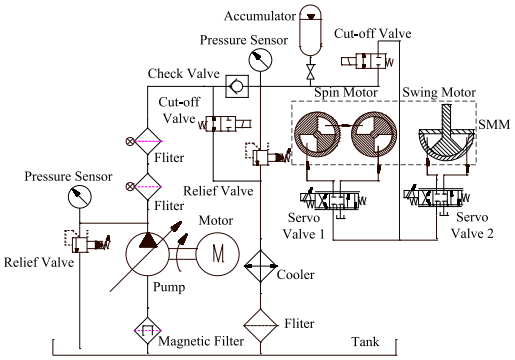

FIGURE 17. Schematic of the hydraulic system.

B. EXPERIMENTAL VERIFICATION

To further explore the designed SMM and validate the control method, experiments are carried out based on the aforementioned theoretical analyses and simulations. The schematic of the hydraulic system used in the test bench is shown in Fig. 17. The test bench, which is composed of a motor, a pump, two servo valves, two encoders, and a servo control module, is shown in Fig. 18. The parameters of the main parts are listed in Table 4.

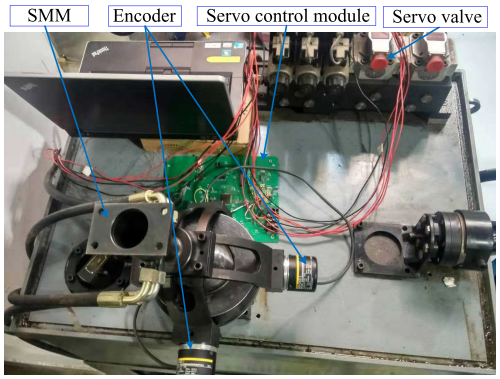

FIGURE 18. Test bench.

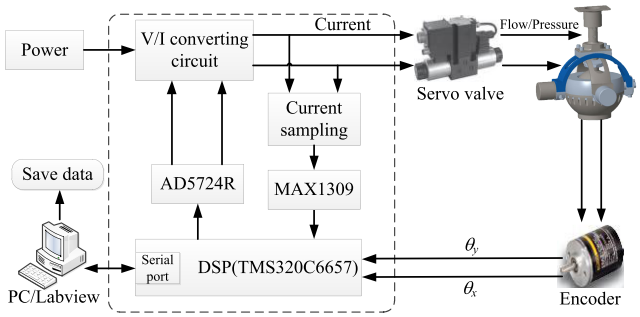

FIGURE 19. Block diagram of control system implementation.

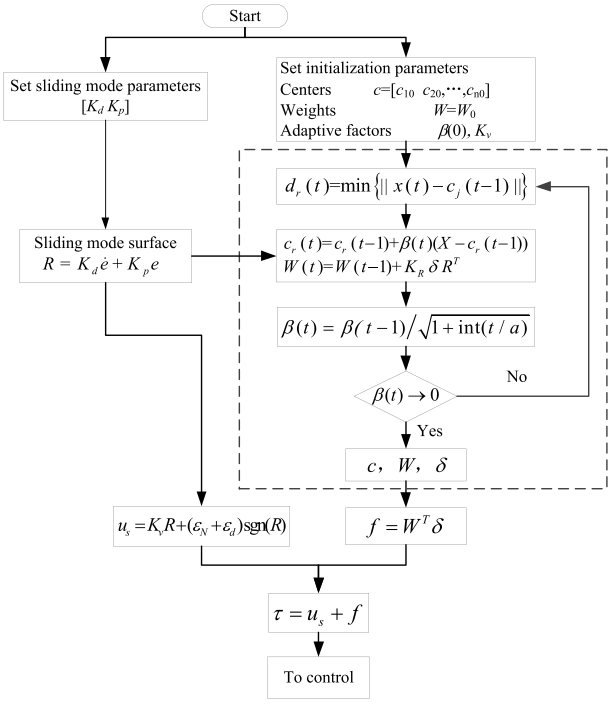

FIGURE 20. RBFSMC program flowchart.

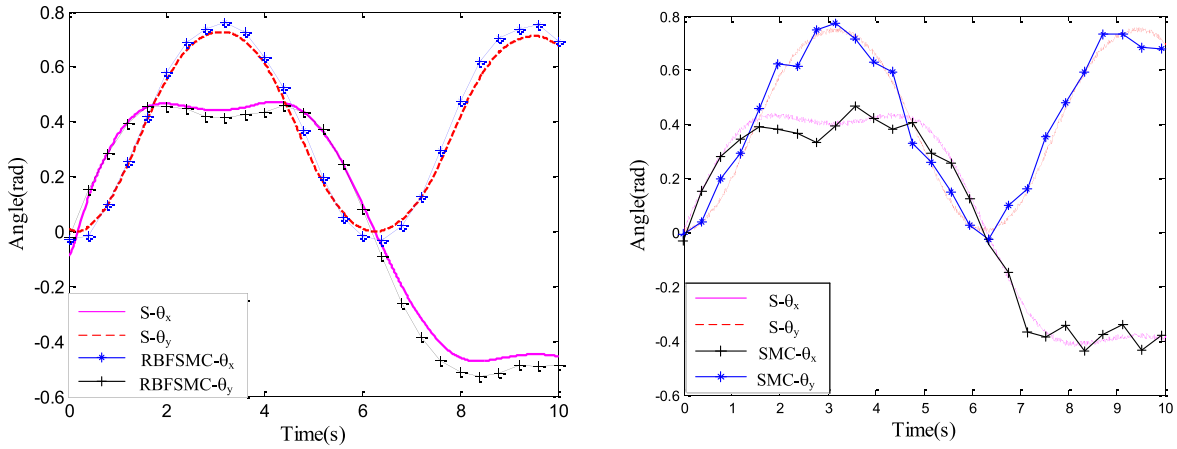

(a) Control performance of RBFSMC

(b) Control performance of SMC

FIGURE 21. Comparison of the simulation and experimental results.

As shown in Fig. 19, the whole control system consists of a host computer and control module. The host computer is employed to communicate with the control module. A graphical user interface (GUI) program is developed in Labview2018 on the host computer. Therefore, the control mode selection, status displaying, control parameters setting, and data acquisition can be easily done through GUI. Moreover, the acquired data is recorded on the host computer, such as the current and rotation angles of the X and Y rails.

The control module consists of a digital signal processor (DSP), D/A, A/D, V/I converter, and current sampling function modules. As the core part of the control module, the DSP TMS320C6657 with two fixed/floating-point processing units and 1.25GHz high speed processing capability is responsible for communicating with computer and algorithm processing. The D/A chip AD5754R can offer 4 channels with 16-bit resolution digital-to-analog converting. The power amplifier OPA549 contained in the V/I converting circuit am employed to convert the analog voltage signals from AD5754R to the current input. The positive and negative supply voltages of OPA549 are set as ± 30 V. The current feedback is obtained by measuring the voltage drop of the current sampling resistor. Then the A/D chip MAX1309 with 4 channels and 12-bit resolution is employed for the digitalization of the voltage signal.

The control algorithm is programmed via C codes in the CCSV6.2. The control program flowchart is shown in Fig. 20.

To evaluate the motion performance of the mechanism, two encoders are used for measuring the rotation angles of the X and Y rails, θ_x and θ_y, respectively. The speed and acceleration of the rotor are zero in the initial state. Equation (58) is selected as the desired trajectory to allow the experimental results to be compared with the simulation results.

A comparison of the simulation and experimental results on the rotation angles of the X and Y rails are shown in Fig. 21(a) and (b), respectively. The maximum errors of θ_x and θ_y using the RBFSMC are approximately 0.07 rad and 0.04 rad respectively, while the SMC gives errors about 0.09 rad and 0.09 rad. Meanwhile, it can be seen that the tracking trajectory using the SMC is fluctuating obviously, while the chattering is almost eliminated when using the RBFSMC.

In summary, the simulation and experimental results are in good agreement. Therefore, the SMM with RBFSMC can smoothly track the desired trajectory with high tracking precision.

VIII. CONCLUSION

This paper presents a novel 2-DOF SMM that can tilt up to $\pm 45°$ and spin 360°. This 2-DOF SMM can be used in robotic applications. Unlike the traditional serial/parallel mechanisms, the proposed SMM with a compact structure, low inertia, and high stiffness is a ball-joint-like hydraulic spherical motion mechanism that can realize continuous 2-DOF rotational motions. The fundamental structure and working principle of the SMM was introduced in detail. Factors that have a bearing on the motion performance, such as workspace and dexterity, were evaluated. Since the system is nonlinear, strongly coupled, and multivariable, the RBFSMC is expected to overcome the influence of imperfect modeling and external disturbance. In addition, the asymptotic stability of the control system was proven. The simulation results showed that the SMM with the RBFSMC can achieve fast response and high tracking precision; moreover, it is highly robust against external disturbance and system uncertainty. Finally, good agreement was observed between the experimental and simulation results, demonstrating the feasibility of the mechanism and the effectiveness of the mathematical models and control method.

This research can provide a new direction and reference point for the design of 2-DOF SMMs.

APPENDIX

The dynamic model of the SMM can be expressed as

$$\mathbf{M}(\mathbf{q})\ddot{\mathbf{q}} + \mathbf{C}(\mathbf{q}, \dot{\mathbf{q}})\dot{\mathbf{q}} + \mathbf{G}(\mathbf{q}) = \tau \tag{A1}$$

The explicit expressions of the terms in the above equation are shown at the top of the next page.

$$\mathbf{M}(\mathbf{q}) = \left(\tan^2\alpha + C^2\beta\right)^{-2} \times \begin{bmatrix} \left(\tan^2\alpha + C^2\beta\right)^2 I_{44} + \sec^2\alpha C^2\beta \begin{bmatrix} I_{55}\sec^2\alpha \\ -I_{11}\left(\tan^2\alpha + C^2\beta\right) \end{bmatrix} & \tan\alpha S\beta C\beta \begin{bmatrix} I_{55}\sec^2\alpha \\ -0.5I_{11}\left(\tan^2\alpha + C^2\beta\right) \end{bmatrix} \\ \tan\alpha S\beta C\beta \begin{bmatrix} I_{55}\sec^2\alpha \\ -0.5I_{11}\left(\tan^2\alpha + C^2\beta\right) \end{bmatrix} & I_{22}\left(\tan^2\alpha + C^2\beta\right)^2 + I_{55}\left(\tan\alpha S\beta\right)^2 \end{bmatrix}$$

$$\mathbf{C}(\mathbf{q}, \dot{\mathbf{q}}) = \sec^2\alpha\left(\tan^2\alpha + C^2\beta\right)^{-3} \times \begin{bmatrix} \sec^3\alpha C\beta \begin{bmatrix} 2S\alpha C\beta\left(I_{11}C^2\alpha S^2\beta - I_{55}\tan^2\alpha\right)\dot{\alpha} \\ +C\alpha S\beta\left(2I_{11}S^2\alpha - I_{55}\tan^2\alpha + I_{55}C^2\beta\right)\dot{\beta} \end{bmatrix} & S\beta C\beta\left(2I_{55}\tan^2\alpha - 0.5I_{11}C^2\beta\right)\dot{\alpha} \\ & + \tan\alpha C^2\beta\left(I_{55}\sec^2\alpha - 0.5I_{11}\right)\dot{\beta} \\ S\beta C\beta\left(I_{55}\sec^4\alpha + 0.5I_{11}\tan^2\alpha\right)\dot{\alpha} & I_{55}S\beta \begin{bmatrix} \tan\alpha S\beta\left(C^2\beta - \tan^2\alpha\right)\dot{\alpha} \\ +S^2\alpha C\beta\left(\sec^2\alpha + S^2\beta\right)\dot{\beta} \end{bmatrix} \\ -\tan\alpha S^2\beta\left(I_{55}\sec^2\alpha - 0.5I_{11}S^2\alpha\right)\dot{\beta} & \end{bmatrix}$$

$$\mathbf{G}(\mathbf{q}) = \begin{bmatrix} 0 \\ -\left(m_b g l_{b0} + m_r g l_{r0} + m_m g l_{m0}\right) S\beta \end{bmatrix}$$

where $I_{11} = I_{m.zz} + 2I_{r.zz}$, $I_{22} = I_{d.xx} + I_{m.xx} + I_{r.xx}$, $I_{33} = I_{d.zz} + I_{m.zz} + I_{r.zz}$, $I_{44} = I_{m.zz}/4 + I_{r.zz}$, $I_{55} = (I_{22} + I_{33})/2$

REFERENCES

[1] R. Kurtz and V. Hayward, "Multiple-goal kinematic optimization of a parallel spherical mechanism with actuator redundancy," *IEEE Trans. Robot. Autom.*, vol. 8, no. 5, pp. 644–651, Oct. 1992.

[2] W. Li and J. Angeles, "Full-mobility 3-CCC parallel-kinematics machines: Forward kinematics, singularity, workspace and dexterity analyses," *Mechanism Mach. Theory*, vol. 126, pp. 312–328, Aug. 2018.

[3] D. Chablat and J. Angeles, "The computation of all 4R serial spherical wrists with an isotropic architecture," *J. Mech. Des.*, vol. 125, no. 2, pp. 275–280, Jun. 2003.

[4] D. Paganelli, "Avoiding parallel singularities of 3UPS and 3UPU spherical wrists," in *Proc. IEEE Int. Conf. Robot. Autom.*, Apr. 2007, pp. 10–14.

[5] G. Wu and S. Bai, "Design and kinematic analysis of a 3-RRR spherical parallel manipulator reconfigured with four–bar linkages," *Robot. Comput.-Integr. Manuf.*, vol. 56, pp. 55–65, Apr. 2019.

[6] G. Palacios MA and O. Alvarez CJ, "The generalized architecture of the spherical serial manipulator," *Adv. Robot. Autom.*, vol. 5, no. 2, pp. 38–45, 2016.

[7] C. M. Gosselin and E. Lavoie, "On the kinematic design of spherical three-degree-of-freedom parallel manipulators," *Int. J. Robot. Res.*, vol. 12, no. 4, pp. 394–402, 1993.

[8] I. A. Bonev and C. M. Gosselin, "Singularity loci of spherical parallel mechanisms," in *Proc. IEEE Int. Conf. Robot. Automat.*, Apr. 2005, pp. 2957–2962.

[9] S. Staicu, "Recursive modelling in dynamics of agile wrist spherical parallel robot," *Robot. Comput.-Integr. Manuf.*, vol. 25, no. 2, pp. 409–416, Apr. 2009.

[10] S. Bai, "Optimum design of spherical parallel manipulators for a prescribed workspace," *Mechanism Mach. Theory*, vol. 45, no. 2, pp. 200–211, Feb. 2010.

[11] K. A. Arrouk, B. C. Bouzgarrou, and G. Gogu, "Workspace characterization and kinematic analysis of general spherical parallel manipulators revisited via graphical based approaches," *Mechanism Mach. Theory*, vol. 122, pp. 404–431, Apr. 2018.

[12] G. Wu, S. Caro, and J. Wang, "Design and transmission analysis of an asymmetrical spherical parallel manipulator," *Mechanism Mach. Theory*, vol. 94, pp. 119–131, Dec. 2015.

[13] M. Karouia and J. M. Hervé, "Asymmetrical 3-dof spherical parallel mechanisms," *Eur. J. Mech.-A/Solids*, vol. 24, no. 1, pp. 47–57, Jan. 2005.

[14] G. Wu and P. Zou, "Comparison of 3-DOF asymmetrical spherical parallel manipulators with respect to motion/force transmission and stiffness," *Mechanism Mach. Theory*, vol. 105, pp. 369–387, Nov. 2016.

[15] S. Leguay-Durand and C. Reboulet, "Optimal design of a redundant spherical parallel manipulator," *Robotica*, vol. 15, no. 4, pp. 399–405, Jul. 1997.

[16] J. Landuré and C. Gosselin, "Kinematic analysis of a novel kinematically redundant spherical parallel manipulator," *J. Mech. Robot.*, vol. 10, no. 2, Apr. 2018, Art. no. 021007.

[17] H. Vincent and R. Kurtz, "Modeling of a parallel wrist mechanism with actuator redundancy," in *Advances in Robot Kinematics*. Vienna, Austria: Springer, 1991, pp. 444–456.

[18] Y. Zhao, F. Gao, W. Li, W. Liu, and X. Zhao, "Development of 6-dof parallel seismic simulator with novel redundant actuation," *Mechatronics*, vol. 19, no. 3, pp. 422–427, Apr. 2009.

[19] L. Wang, J. Wu, and J. Wang, "Dynamic formulation of a planar 3-DOF parallel manipulator with actuation redundancy," *Robot. Comput.-Integr. Manuf.*, vol. 26, no. 1, pp. 67–73, Feb. 2010.

[20] M. Zein, P. Wenger, and D. Chablat, "Non-singular assembly-mode changing motions for 3-RPR parallel manipulators," *Mechanism Mach. Theory*, vol. 43, no. 4, pp. 480–490, Apr. 2008.

[21] V. Hayward, "Design of a hydraulic robot shoulder based on a combinatorial mechanism," in *Experimental Robotics III*. Berlin, Germany: Springer, 1994, pp. 295–309.

[22] T. A. Hess-Coelho, "A redundant parallel spherical mechanism for robotic wrist applications," *J. Mech. Des.*, vol. 129, no. 8, pp. 891–895, Aug. 2007.

[23] H. Saafi, M. A. Laribi, and S. Zeghloul, "Optimal torque distribution for a redundant 3-RRR spherical parallel manipulator used as a haptic medical device," *Robot. Auto. Syst.*, vol. 89, pp. 40–50, Mar. 2017.

[24] S. Liu, G. Peng, and H. Gao, "Dynamic modeling and terminal sliding mode control of a 3-DOF redundantly actuated parallel platform," *Mechatronics*, vol. 60, pp. 26–33, Jun. 2019.

[25] Y. X. Su, B. Y. Duan, and C. H. Zheng, "Nonlinear PID control of a six-DOF parallel manipulator," *IEE Proc.-Control Theory Appl.*, vol. 151, no. 1, pp. 95–102, Jan. 2004.

[26] A. K. Kadam, D. D. Ray, S. R. Shimjith, P. D. Shendge, and S. B. Phadke, "Time delay controller combined with sliding mode for DC motor position control: Experimental validation on quanser QET," in *Proc. Int. Conf. Power, Energy Control (ICPEC)*, Feb. 2013, pp. 449–453.

[27] A. Durdu and E. H. Dursun, "Sliding mode control for position tracking of servo system with a variable loaded DC motor," *Elektronika ir Elektrotechnika*, vol. 25, no. 4, pp. 8–16, 2019.

[28] M. Wei and G. Chen, "Adaptive RBF neural network sliding mode control for ship course control system," in *Proc. 3rd Int. Conf. Intell. Hum.-Mach. Syst. Cybern.*, Aug. 2011, pp. 27–30.

[29] T. Sun, H. Pei, Y. Pan, H. Zhou, and C. Zhang, "Neural network-based sliding mode adaptive control for robot manipulators," *Neurocomputing*, vol. 74, nos. 14–15, pp. 2377–2384, Jul. 2011.
[30] A. Sharafian, V. Bagheri, and W. Zhang, "RBF neural network sliding mode consensus of multiagent systems with unknown dynamical model of leader-follower agents," *Int. J. Control, Autom. Syst.*, vol. 16, no. 2, pp. 749–758, Apr. 2018.

BIN BIAN received the master's degree from Yanshan University, China, in 2013. He is currently pursuing the Ph.D. degree in mechanical engineering with Beihang University, Beijing, China. His research interests include robotic structure and control and hydraulic power transmission and control.

LIANG WANG received the B.S. degree from the Harbin Shipbuilding Engineering Institute, in 1985, the M.S. degree from the Harbin Institute of Technology, in 1988, and the Ph.D. degree from Beihang University, in 2000. He is currently a Professor and the Supervisor of Ph.D. Student with Beihang University. His main research interests include robotic structure and control, human–machine system, mechatronics, and hydraulic power transmission and control.